Available online at www.sciencedirect.com
SCIENCE DIRECT®
International Journal of Heat and Mass Transfer 49 (2006) 4496–4510
International Journal of HEAT and MASS TRANSFER
www.elsevier.com/locate/ijhmt

Chemical non-equilibrium modelling of columnar solidification

P. Roux [a,b], B. Goyeau [b,*], D. Gobin [b], F. Fichot [a], M. Quintard [c]

[a] Institut de Radioprotection et de Sûreté Nucléaire C.E.A Cadarache, Bât. 700, 13108 Saint Paul Lez Durance, France
[b] Laboratoire FAST – Universités Paris VI et Paris XI – UMR CNRS 7608. Bât. 502, Campus Universitaire, 91405 Orsay Cedex, France
[c] Institut de Mécanique des Fluides de Toulouse Avenue du Professeur Camille Soula, 31400 Toulouse, France

Received 21 November 2005; received in revised form 21 May 2006
Available online 25 July 2006

Abstract

This paper deals with the macroscopic modeling and numerical simulation of columnar dendritic solidification of binary alloys. The macroscopic governing equations and associated effective transport properties were previously derived using a volume averaging technique with local closure. The macroscopic model takes into account the spatial variation of the pore-scale geometry within the mushy zone, which leads to additional terms involving porosity gradients. The second important feature concerns solute mass conservation, which is described by considering a macro-scale non-equilibrium accounting for chemical exchanges at the solid–liquid interface. A simplified version of the model is validated through a comparison of the numerical solution to three experiments available in the literature. Porosity extra terms are systematically estimated on the basis of these numerical simulations, and the influence on solidification of effective transport properties such as permeability and interfacial solute exchange coefficients is investigated.

1. Introduction

Solidification phenomena are encountered in a wide range of industrial applications often related to metallurgy (casting, welding,...) or in natural situations such as freezing, magmatic crystallization, or snow formation. They are also involved in the nuclear security context where the corium multi-component mixture possibly resulting from severe accident needs to be rapidly solidified [1]. For this reason, solidification modeling of multi-component mixtures has been the subject of intense research activity in the last decades and one of the most challenging problems lie in the coupling of phenomena occurring at different length scales [2]. Indeed, in columnar dendritic solidification, heat and mass transfer in both liquid and solid phases are coupled by the transient development of the "mushy zone". It is necessary to have an accurate description of transport phenomena within this mushy zone where the interdendritic liquid flow and local heat and solute transport processes play a key role on the micro-macro-segregation, and, therefore, on the final product quality.

Usually, the dendritic mushy zone is described as a porous medium [3] and macroscopic conservation equations have been obtained using mixture theory [4–7] or up-scaling methods such as homogenization [8,9] or volume averaging methods [10]. Since the complexity of local geometry and physical phenomena may be included in averaged conservation equations through effective transport properties, the method of volume averaging has been often chosen [11–16] in the solidification context. Homogenization and averaging procedures require scale separation between the pore scale and the porous medium scale. It seems that this requirement is not satisfied in the case of dendritic zones, where local geometry evolves continuously. This has been studied thoroughly, using actual description of mushy zones, and it has been shown that continuous spatial variations of the geometry of the dendrites (evolving heterogeneities) are most of the time "moderate", the scale separation in the mushy zone remaining satisfied [17]. Actually, accounting for these evolving heterogeneities

* Corresponding author.
E-mail address: goyeau@fast.u-psud.fr (B. Goyeau).

0017-9310/$ - see front matter © 2006 Elsevier Ltd. All rights reserved.
doi:10.1016/j.ijheatmasstransfer.2006.05.020

Nomenclature

A_k	interfacial solid–liquid area concentration (m^{-1})
C_k	volume average concentration in phase k
C_{pk}	Massic heat capacity of phase k ($J\,kg^{-1}\,K^{-1}$)
D_k	molecular diffusion coefficient in phase k ($m^2\,s^{-1}$)
$\mathbf{D}_\ell$	effective diffusion–dispersion tensor ($m^2\,s^{-1}$)
$\mathbf{F}$	Forchheimer correction
$\vec{g}$	gravity ($m\,s^{-2}$)
H	Massic enthalpy ($J\,kg^{-1}$)
H	height of the experimental domain (m)
h_{m_k}	interfacial species exchange coefficients in phase k (s^{-1})
$\mathbf{K}$	permeability tensor (m^2)
ℓ	index for liquid phase
L_M	macroscopic length scale of the mushy zone (m)
L_a	latent heat ($J\,kg^{-1}$)
L	width of the experimental domain (m)
ℓ_β	primary interdendritic length scale (m)
ℓ_k	characteristic length scale of the mushy zone (m)
P_ℓ	pressure in liquid phase (Pa)
Pe	Péclet number
Q	volumic heat generation ($W\,kg^{-1}$)
R_0	characteristic size of the averaging volume (m)
s	index for solid phase
T	temperature (K)
t	time (s)
$\vec{V}_\ell$	liquid velocity ($m\,s^{-1}$)

Notations

$\langle . \rangle^k$	intrinsic volume average in phase k
$\tilde{.}$	fluctuation
*	notation for thermodynamical equilibrium

Greek symbols

β_T	thermal expansion coefficient (K^{-1})
β_C	solutal expansion coefficient
ε_k	volume fraction of phase k
μ_ℓ	dynamic viscosity in liquid phase ($Pa\,s^{-1}$)
Λ_{eff}	effective conductivity tensor ($W\,m^{-1}\,K^{-1}$)
λ	thermal conductivity ($W\,m^{-1}\,K^{-1}$)
λ_1	primary dendritic arm spacing (m)
λ_2	secondary dendritic arm spacing (m)
ρ_k	density of phase k ($kg\,m^{-3}$)

provides additional terms in the macro-scale equations that include porosity gradients [18–21] whose influence on macroscopic fields has to be analyzed.

Besides the difficulty associated to the evolving geometry, another important difficulty in solidification modeling lies in species transport, characterized by very different molecular diffusivities in the liquid and solid phases. This is known to give many different macro-scale models, depending on the relative importance of the pore scale transport properties. In most existing models, the solute transport has been macroscopically described using only one conservation equation, assuming the mass diffusion rate in the solid phase to be extremely fast (lever rule) [11,22,23] or very slow (Scheil's description) [7,24,25]. Recently, a non-equilibrium description of the solute transport has been proposed, with the interfacial mass exchange term being proportional to the difference between interfacial and volume-averaged concentrations [13,26]. In this formulation, the mass exchange coefficient was found to be mainly dependent on the diffusion length [27], while it has been shown that it also depends on tortuosity and local dispersion phenomena [26].

At the time, papers have been published about the implementation and use of numerical models associated to some of the macro-scale models described above [14,27–29]. The above discussion has indicated the possible influence of model additional features, such as: (i) the impact of the geometrical complexity of the mushy on macro-scale equations and effective properties, (ii) the introduction of *chemical non-equilibrium* mass transfer between the liquid and solid phases during phase change.

This is the objective of this paper to discuss the impact of these additional features on the macroscopic modeling of *non-homogeneous* columnar dendritic solidification. After a brief presentation of the macroscopic model, a numerical validation of a simplified version of this model is obtained by comparison with three solidification experiments [29–31]. The porosity extra terms are estimated on the basis of the numerical results, and this allows to discuss the validity of the proposed simplifications. Finally, the influence of effective transport properties such as permeability and interfacial solute exchange coefficients on the solidification process is investigated.

2. Macroscopic model

The macroscopic solidification model has been derived using the volume average of the local problem describing mass, momentum, energy and species conservation, in both solid and liquid phases and at the solid–liquid interface [18,26,32]. The set of pore-scale equations is integrated over an averaging volume, whose size R_0 is supposed to be large compared to the primary interdendritic length scale l_β but small compared to the macroscopic length scale of the mushy zone L_M. Such an upscaling method has been extensively discussed in the porous media literature [10] and will not be presented in this section. All details concerning the derivation of the macroscopic model are

provided in several papers [18,26,32] and, for conciseness, only the main characteristics of the model are presented in relation to the numerical simulations performed in Sections 3–5.

2.1. Geometrical considerations

As indicated in the introduction, the volume averaging method is usually valid for homogeneous porous structures for which scale separation between the different length scales is satisfied. In columnar dendritic regions, the situation is much more complex due to continuous spatial variations (evolving heterogeneities) of the pore-scale geometry, and therefore the average transport properties. In this case, scale separation depends on the spatial geometry variations which may be characterized by a geometry decrease rate as in [17]. In this paper, it was found that, for large evolving heterogeneities, averaging without any scale separation would lead to non-local terms and very complex models. For lower geometry rate of variation, additional terms containing porosity gradients must be included in the analysis, at the expense of more complexity. For moderate rates of variation, it is expected that the traditional form of the equations may be retained, with effective parameters being macroscopically heterogeneous [17]. As emphasized in this reference, most dendritic structures seem to have moderate evolving heterogeneities. However, the possible influence of the additional porosity gradient terms has not been quantitatively investigated, and this will be one of the objectives of this paper. Before proceeding to the description of the macro-scale model, it must be emphasized that an alternative to the one-domain representation (i.e., a continuous description going from the solid to the mush then the liquid) exists. A two-domain approach may be introduced, with macroscopic models in both the solid and liquid regions coupled at the interface by jump boundary conditions following ideas put forth in [33–35]. In this approach, mushy zone effects are dealt with macro-scale jump coefficients, and we believe that it is still a challenge to incorporate this physical description in such a lumped model. While it cannot be rejected at this point, this is beyond the scope of this paper to explore this route.

2.2. Macroscopic model

In this section the macroscopic conservation equation for mass, momentum, solute, energy and solidification rate are presented and commented. The associated closure problems have been previously presented [18] and will not be repeated here.

Mass conservation

$$\frac{\partial}{\partial t}(\varepsilon_\ell \rho_\ell) + \nabla.(\varepsilon_\ell \rho_\ell \langle \vec{V}_\ell \rangle^\ell) = \underbrace{-\frac{\partial}{\partial t}(\varepsilon_s \rho_s)}_{\text{Solidification rate}} \tag{1}$$

where the right hand side (RHS) of Eq. (1) stands for the solidification rate.

Momentum conservation

$$\begin{aligned}\frac{\partial}{\partial t}(\varepsilon_\ell \rho_\ell \langle \vec{V}_\ell \rangle^\ell) + \nabla.(\varepsilon_\ell \rho_\ell \langle \vec{V}_\ell \rangle^\ell \langle \vec{V}_\ell \rangle^\ell) &= -\varepsilon_\ell \vec{\nabla} \langle P_\ell \rangle^\ell + \varepsilon_\ell \mu_\ell \nabla^2 \langle \vec{V}_\ell \rangle^\ell + \mu_\ell \vec{\nabla} \varepsilon_\ell . \vec{\nabla} \langle \vec{V}_\ell \rangle^\ell \\ &\quad + \mu_\ell (\nabla^2 \varepsilon_\ell) \langle \vec{V}_\ell \rangle^\ell + \varepsilon_\ell \rho_\ell \vec{g} - \varepsilon_\ell^2 \mu_\ell \mathbf{K}^{-1} . \langle \vec{V}_\ell \rangle^\ell \\ &\quad - \varepsilon_\ell^2 \mu_\ell \mathbf{K}^{-1} . \mathbf{F} . \langle \vec{V}_\ell \rangle^\ell \end{aligned} \tag{2}$$

In Eq. (2) the dispersive flux $\nabla.(\varepsilon_\ell \rho_\ell \langle \widetilde{\vec{V}_\ell} \widetilde{\vec{V}_\ell} \rangle^\ell)$ has been neglected since it as been shown to be much lower than the convective and friction terms in the liquid and mushy regions, respectively [32]. The next to the last term of Eq. (2) is the Darcy's term where $\mathbf{K}$ is the permeability tensor while the last term represents the Forchheimer correction where $\mathbf{F}$ is an inertia tensor. Local closure problems have been derived for their determination [19,21,36] and numerical solutions for $\mathbf{K}$ in the context of columnar dendritic structures have been obtained [37,38]. In Eq. (2), $\varepsilon_\ell \mu_\ell \nabla^2 \langle \vec{V}_\ell \rangle^\ell$ is the first Brinkman correction term while $\mu_\ell \vec{\nabla} \varepsilon_\ell . \nabla \langle \vec{V}_\ell \rangle^\ell$ and $\mu_\ell (\nabla^2 \varepsilon_\ell) \langle \vec{V}_\ell \rangle^\ell$ represent the second Brinkman correction related to the heterogeneity of the dendritic porous structure [17,38]. Actually, these terms are expected to be negligible in the core of the mushy zone while they should have a significant influence in the vicinity of the tip of the dendrites. These extra terms will be numerically quantified in the next section. Rigorously, this spatial porosity dependence leads to non-local closure problems whose determination remains a challenge. However, on the basis of scale separation it has been shown that these "source terms" in the deviation problems are small and therefore classical boundary value problems can be used in dendritic structures [17,18,38].

Solute conservation

As previously said, the macroscopic solidification model is characterized by chemical non-local equilibrium, i.e., the macroscopic concentrations may not be linked directly by the micro-scale thermodynamic equilibrium condition valid at the solid–liquid interface. Under these circumstances [26], the macroscopic solute transport is represented by two average equations

Solid phase

$$\begin{aligned}\frac{\partial}{\partial t}(\varepsilon_s \rho_s \langle C_s \rangle^s) - C_s^* \frac{\partial}{\partial t}(\varepsilon_s \rho_s) &= \nabla.(\varepsilon_s \rho_s D_s \vec{\nabla} \langle C_s \rangle^s) + \underbrace{\rho_s h_{m_s} (C_s^* - \langle C_s \rangle^s)}_{\text{Interfacial mass exchange}} \\ &\quad - \rho_s D_s (\vec{\nabla} \varepsilon_s) . \vec{\nabla} \langle C_s \rangle^s - \nabla.(\rho_s D_s (\vec{\nabla} \varepsilon_s)(C_s^* - \langle C_s \rangle^s)) \end{aligned} \tag{3}$$

Liquid phase

$$\begin{aligned}\frac{\partial}{\partial t}(\varepsilon_\ell \rho_\ell \langle C_\ell \rangle^\ell) + \nabla.(\varepsilon_\ell \rho_\ell \langle C_\ell \rangle^\ell \langle \vec{V}_\ell \rangle^\ell) + C_\ell^* \frac{\partial}{\partial t}(\varepsilon_s \rho_s) &= \nabla.\varepsilon_\ell \rho_\ell \mathbf{D}_\ell \vec{\nabla} \langle C_\ell \rangle^\ell - \rho_\ell \mathbf{D}_\ell (\vec{\nabla} \varepsilon_\ell) . \vec{\nabla} \langle C_\ell \rangle^\ell \\ &\quad + \underbrace{\rho_\ell h_{m_\ell} (C_\ell^* - \langle C_\ell \rangle^\ell)}_{\text{Interfacial mass exchange}} - \nabla.(\rho_\ell \mathbf{D}_\ell (\vec{\nabla} \varepsilon_\ell)(C_\ell^* - \langle C_\ell \rangle^\ell)) \end{aligned} \tag{4}$$

where interfacial mass exchange, expressed in terms of the difference between interfacial $(C_k^*, k = l, s)$ and volume-average concentrations ($\langle C_k \rangle^k$, $k = l,s$), and porosity gradient terms are included. In the interfacial terms, coefficients h_{ms} and $h_{m\ell}$ are obtained from the associated local closure problems which have been numerically solved using schematic and digitized columnar dendritic structures [26]. The results have shown the dependence of these coefficients both on the liquid volume fraction and the local Péclet number. In Eqs. (3) and (4) D_s and D_ℓ are the molecular diffusion coefficients in the solid and liquid phases, respectively, while $\mathbf{D}_\ell$ represents the effective diffusion–dispersion tensor depending on the local structure but also on the local flow intensity. Actually, this *active dispersion model* is found to be less sensitive to the local Peclet number than the *passive dispersion* representation, where no diffusion in the solid is assumed [39]. This is due to the impact of the boundary condition at the solid–liquid interface: Dirichlet condition in the active case and Neumann condition in the passive model. In this latter case, since no exchange is possible at the solid–liquid interface, tortuosity effects are also present in the effective diffusion tensor [39].

2.2.1. Energy conservation

Since thermal diffusivity is much higher than the molecular difusivity, the assumption of local thermal equilibrium is acceptable [40–42]. Therefore, macroscopic energy conservation is governed by only one average equation whose representation in terms of enthalpy is given by

$$\begin{aligned}&\frac{\partial}{\partial t}(\rho\langle H\rangle) + \nabla.(\varepsilon_\ell \rho_\ell \langle H_\ell\rangle^\ell \langle \vec{V}_\ell\rangle^\ell)\\ &\quad - \sum_{k=\ell}^{s}\sum_{i=\alpha}\beta[\langle H^i\rangle^k \rho_k D_k.\vec{\nabla}\langle C_k^i\rangle^k]\\ &\quad + \sum_{k=\ell}^{s}\sum_{i=\alpha}\beta[\langle H^i\rangle^k \rho_k D_k(\vec{\nabla}\varepsilon_k)(C_k^{i^*} - \langle C_k^i\rangle^k)]\\ &\quad = \nabla.(\Lambda_{\text{eff}}.\vec{\nabla}\langle T\rangle) + \langle\rho\rangle\langle\dot{Q}\rangle \end{aligned} \tag{5}$$

where Λ_{eff} is the effective conductivity tensor taking into account both tortuosity and local dispersion effects [18].

2.2.2. Solidification rate

The solidification rate in Eqs. (1), (3) and (4) is obtained by averaging the species mass balance equation at the solid–liquid interface. Its macroscopic form is given by

$$\begin{aligned}\frac{\partial}{\partial t}(\varepsilon_s\rho_s) = \frac{1}{C_\ell^* - C_s^*}[&\rho_s h_{m_s}(C_s^* - \langle C_s\rangle^s) + \rho_\ell h_{m_\ell}(C_\ell^* - \langle C_\ell\rangle^\ell)\\ &- \rho_s D_s(\vec{\nabla}\varepsilon_s).\vec{\nabla}\langle C_s\rangle^s - \rho_\ell D_\ell(\vec{\nabla}\varepsilon_\ell).\vec{\nabla}\langle C_\ell\rangle^\ell]\end{aligned} \tag{6}$$

where interfacial mass exchange terms and porosity gradient are involved.

3. Simplified model and numerical validation

The macroscopic model derived in the previous section leads to a set of equations including a number of non-classical terms, in particular, extra terms arising from the porosity gradients, and a two-equation formulation for species conservation. Due to the complexity of this model, a simplified version, without the extra terms, but still based on the chemical non-equilibrium representation, is proposed. These extra terms involving porosity gradients are discarded on the base of estimates (Section 5). The simplified model is numerically solved and results are compared to experiments and numerical results available in the literature.

3.1. Simplified model

The simplified model is based on the following assumptions:

(1) The Boussinesq approximation is considered: the density is such that $\rho_l = \rho_0$ everywhere in the equations, except in the gravity term in the momentum equation, where a linear approximation is used

$$\rho_l = \rho_0(1 - \beta_T(\langle T\rangle - T_{\text{ref}}) - \beta_C(\langle C_\ell\rangle^\ell - C_{\text{ref}})) \tag{7}$$

(2) Permeability variation with porosity is given by an isotropic Kozeny–Carman law [43]

$$K = \frac{l_k^2}{180}\frac{\varepsilon_\ell^3}{(1-\varepsilon_\ell)^2} \tag{8}$$

where the "pore size" l_k is a characteristic length of the mushy zone [16,22,23,44]. The primary dendritic arm spacing λ_1 is generally used when the flow is parallel to the axis of the dendrites, and the secondary arm spacing λ_2 when the fluid velocity is orthogonal. For the situations under consideration in this analysis, the secondary arm seems to be more adapted [45,46] although other correlations could be used.

(3) The interfacial species coefficients are assumed to be dependent on the solid–liquid specific area A_k such as

$$h_{mk} = \frac{A_k D_k}{l_k} \quad \text{and} \quad A_k = \frac{12}{\varepsilon_k l_k} \tag{9}$$

Expression (9) has been obtained for simple geometric structures in purely diffusive situations by Wang and Beckermann [47]. Let us note that a similar form has also been obtained by solving the closure problems for stratified systems [48]. In the following calculations, $l_k = \lambda_2$ leading to

$$h_{mk} = 12\frac{D_k}{\lambda_2^2\varepsilon_k} \tag{10}$$

(4) Rigourously speaking, the effective conductivity tensor of the dendritic mushy zone is composed of an average diffusion term $\lambda_{\text{eq}} = \varepsilon_s\lambda_s + \varepsilon_\ell\lambda_\ell$ and of both

dispersion and tortuosity contributions. However, in the absence of an accurate estimation of dispersion effects, and due to the small differences between the phase conductivities, both contributions are neglected in the present model. In Table 2 some typical values of thermal conductivities corresponding to the different components of the alloys under consideration in the test-cases are provided.

3.2. Numerical procedure

The numerical approximation of the conservation equations was performed by using a finite volume method. The set of differential partial equations is characterized first by non-linearities and by the strong coupling of the equations. This makes difficult the resolution of the system and the most robust solution would probably to use an implicit scheme involving all unknown variables. However, in order to save computational time, a semi-implicit three steps resolution was developed. The first step consists in the resolution of the Navier–Stokes equations with a Simple algorithm. Then, the energy conservation equation is solved using the previously calculated velocity field and finally, the solidification rate is calculated together with the species conservation in the liquid and solid phases, in the same linear system. This procedure is iterated until convergence of all the macroscopic fields.

3.3. Description of the test cases

The accuracy of the numerical code is evaluated by comparing the numerical results to experimental results available in the literature. Note that, because of the experimental difficulties, only few experiments related to solidification of binary alloys have been published. Three of them, concerning metallic alloys, have been selected for the present validation. In the three cases, a parallelepipedic cavity is considered and the initial melt (at uniform concentration and temperature) is cooled from one vertical side wall, the other boundaries being assumed as adiabatic (Fig. 1). Let us present in details the selected experimental cases.

3.3.1. Lead–tin experiments

These experiments have been performed by Hebditch and Hunt [30] with Pb–Sn mixtures and the results have been used in Ahmad et al. [29] for a validation exercise of two macroscopic solidification models: the FEM code developed by Rappaz and coworkers [49] and the FVM code implemented by Combeau and colleagues [50]. Two different initial compositions have been considered: a 48% lead alloy (experiment A) and a 5% tin alloy (experiment B). In both cases, macro-segregation has been observed at the end of the ingot solidification and temperature evolutions were measured at various locations. The properties corresponding to the mixture are given in Table 1 and a simplified phase diagram of Pb–Sn alloys is presented in Fig. 2. The heat flux extracted from the left side of the domain is assumed to be given by a uniform heat exchange coefficient with the outside at a constant temperature.

Table 1
Physical properties of metal alloys

		Pb(48%)–Sn	Pb–Sn(5%)	Bi(10%)–Sn
C_{p_ℓ}, C_{p_s}	J kg^{-1} K^{-1}	200	260	250
λ_ℓ, λ_s	W m^{-1} K^{-1}	50	55	60
L_a	J kg^{-1}	53,550	61,000	59,430
ρ_ℓ, ρ_s	kg m^{-3}	9000	7000	7550
β_T	K^{-1}	10^{-4}	6×10^{-5}	$9\times5\times10^{-5}$
β_C		0.45	−0.053	-3×10^{-3}
μ_ℓ	kg m^{-1} s^{-1}	10^{-3}	10^{-3}	1.85×10^{-3}
D_ℓ	m^2 s^{-1}	1×10^{-9}	1×10^{-9}	1.8×10^{-9}
D_s	m^2 s^{-1}	1×10^{-13}	1×10^{-13}	1×10^{-13}
λ_1	μm	350	200	1000
λ_2	μm	40	65	300
T_{ini}	K	489	499	500
h	W m^{-2} K^{-1}	400	300	∞
T_{out}	K	298	298	−2 K min^{-1}
H	cm	6	6	6
L	cm	10	10	5

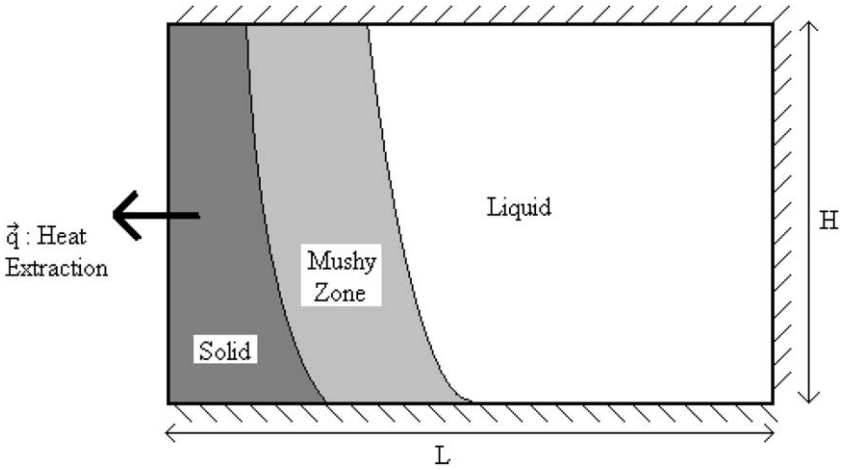

Fig. 1. Experimental configuration for the reference experiments.

Table 2
Conductivity for differents metals

		Pb	Sn	Bi	Bi–Sn
T_{fusion}	K	600	500		
λ_s ($T = 300$ K)	W/m K	35.3	66.6	7.87	
λ_s ($T = 500$ K)		32.8	59.6		
λ_ℓ ($T = 500$ K)			30		30
λ_ℓ ($T = 600$ K)		15	32		
λ_ℓ ($T = 1000$ K)		20	32		

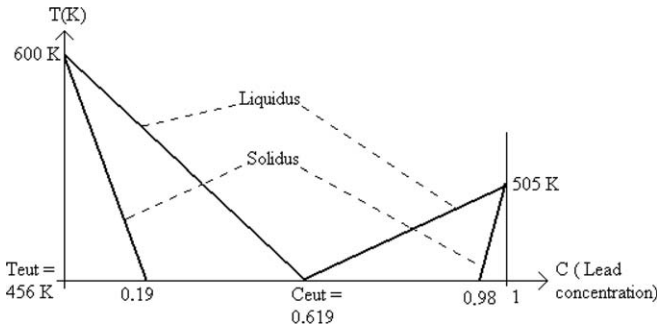

Fig. 2. Phase diagram of Pb–Sn melt.

3.3.2. Bismuth–tin experiment

A Bi(10%)–Sn experiment was performed by Quillet [31] (experiment C) . In the experimental device, the extracted heat flux was monitored in order to decrease the cold wall temperature at a constant rate. The temperature field was measured at different times in various locations. A *post-mortem* analysis of the ingot was performed to obtain the macrosegregation field. In this section, the comparison is provided for a cooling rate of 2 K min^{-1}. The simplified phase diagram of hypoeutectic Bi–Sn alloys is presented in Fig. 3. For all the three cases the physical properties, the geometry and boundary conditions are summarized in Table 1.

3.4. Comparison results

The comparison of the experimental results with the numerical simulations performed with the simplified model are presented below.

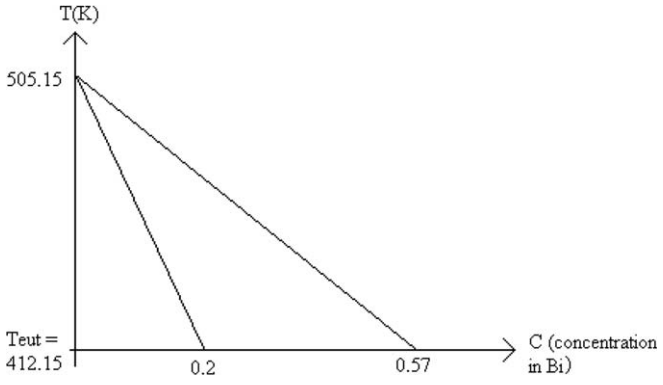

Fig. 3. Phase diagram of Bi–Sn.

3.4.1. Experiment A (Sn–48% Pb)

In this case, the solutal buoyancy force is in opposition with the thermal buoyancy force. As the solutal effect is dominant, we observe an inversion of the convective motion after the beginning of solidification during which thermal convection is dominating, and the circulation loop is ascending along the cold wall. This is illustrated in Fig. 4 which represents streamlines obtained with the present code and by the FVM code presented by Ahmad et al. (after 50 s of solidification). It is shown that the streamlines obtained with this model are qualitatively similar, but present some differences in the shape and the location of the center of the vortex. We may expect these differences to come from the different treatment of species conservation. Indeed, in Ahmad et al. a single concentration formulation is used and species diffusion is neglected. This may influence the buoyancy forces and therefore the intensity of natural convection.

In Fig. 5, the results are presented in terms of iso-concentration lines at $t = 400$ s, in order to allow for the comparison with the results of the FVM code (Ahmad et al. [29]). Both calculations show a solute enrichment in the upper part of the domain resulting from the solute redistribution. We find a good qualitative agreement with the FVM simulations reported in [29] and with Hebditch and Hunt experimental results [30]. It can be noticed in the concentration field obtained with the present model

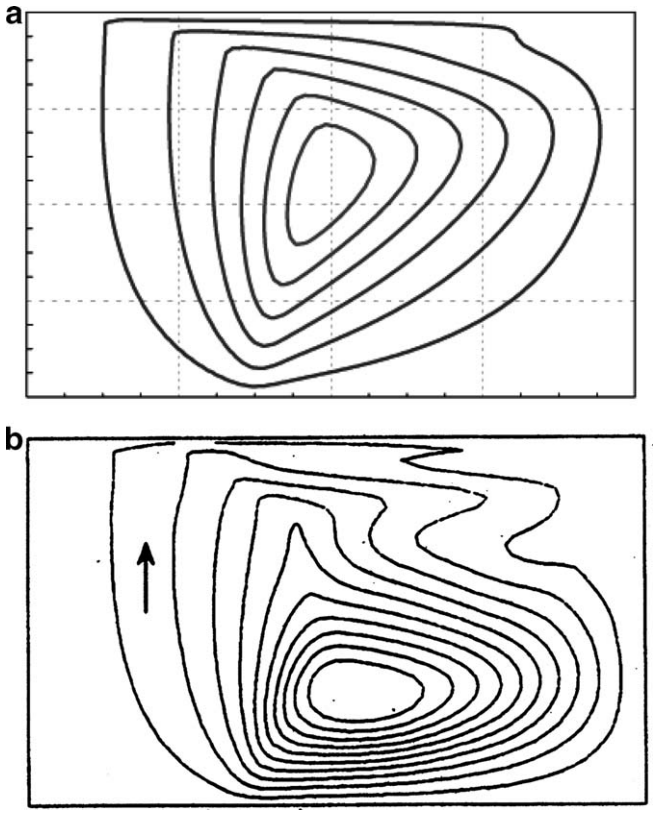

Fig. 4. Streamlines ($\Delta\psi = 3.67 \times 10^{-6}$) after 50 s of solidification for experiment A: (a) our model and (b) FVM code in Ahmad et al. [29].

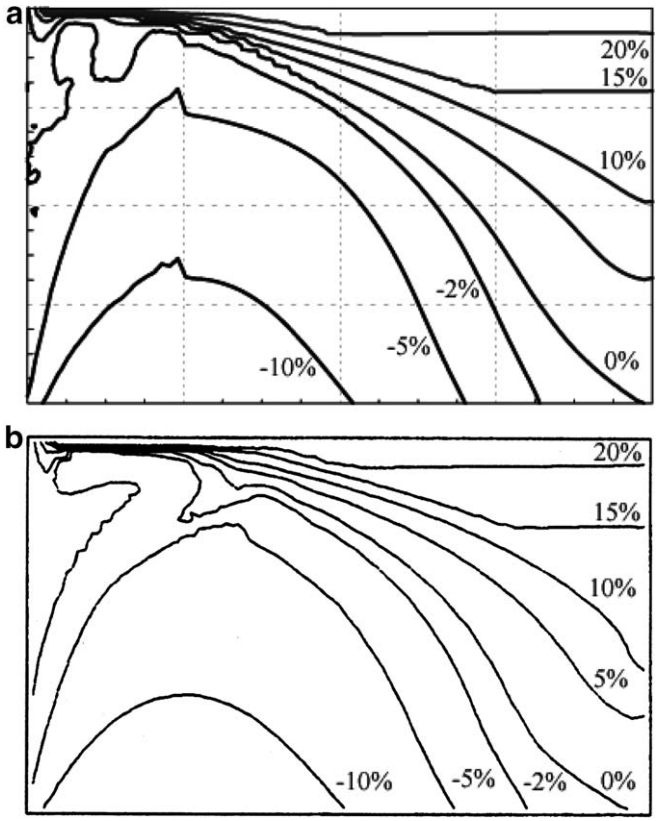

Fig. 5. Concentration enrichment isovalues in % after 400 s of solidification for experiment A: (a) our model and (b) FVM code in Ahmad et al. [29].

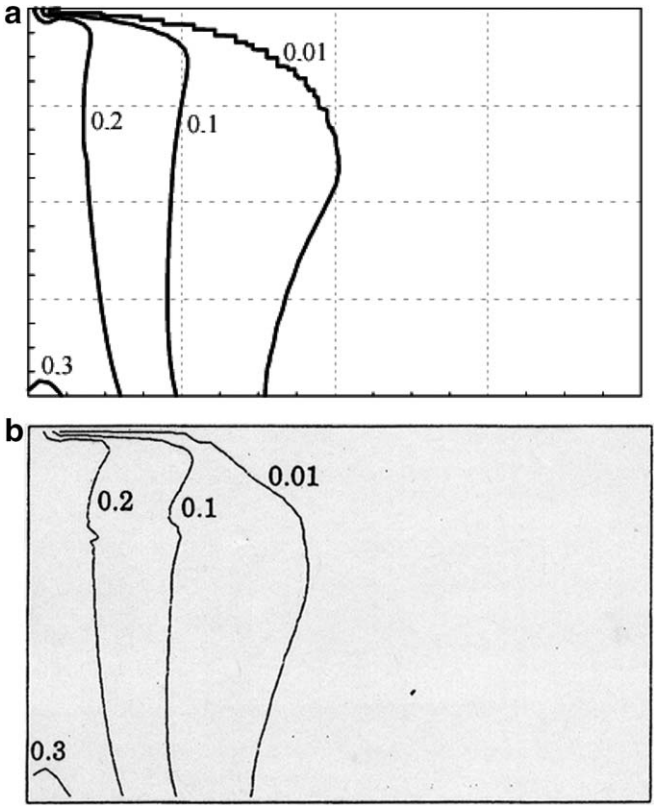

Fig. 6. Solid fraction isovalues after 50 s of solidification for experiment A: (a) our model and (b) FVM code in Ahmad et al. [29].

that the -5% and -10% isovalues present an angular shape. This can be due to the presence of a strong jump of solid volume fraction from 0.4 to 1. On the other hand, let us note the formation of a thin liquid channel, enriched in solute, at the top of the cavity. This is illustrated in Fig. 6 where the solid fraction isovalue of 0.01 at $t = 50$ s delimits the liquid zone. A good agreement between the present calculations and those reported in [29] is observed. In order to deal with the strong gradients in this upper region a refined mesh has been used. A 60 horizontal $\times$ 36 vertical mesh was used, with a refinement at the top: the function $H\sin(\pi/2)(i-1)/(37)$ was used for defining the ith position of the vertical sides of the meshes.

3.4.2. Experiment B: (Pb–5% Sn)

In this case, the solutal expansion coefficient is negative, and the solutal and thermal effects are cooperating. As a consequence, the circulating fluid is moving down along the cold wall and then up along the solid. In Fig. 7 the streamlines obtained with the present model are compared to the FVM code presented in Ahmad et al. In order to provide a quantitative comparison with the results by Hebditch and Hunt [30] and Ahmad et al. [29], the results are displayed at $t = 100$ s. This case is first characterized by a mushy zone of large extension, and second by the existence of a liquid channel at the bottom of the cavity where

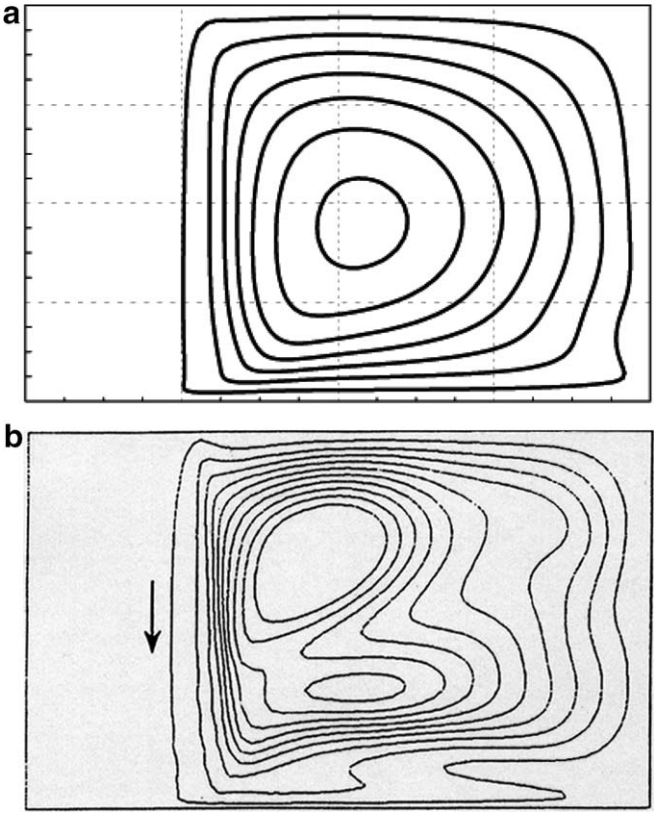

Fig. 7. Streamlines ($\Delta\psi = 1.56 \times 10^{-6}$) after 100 s of solidification for experiment B: (a) our model and (b) FVM code in Ahmad et al. [29].

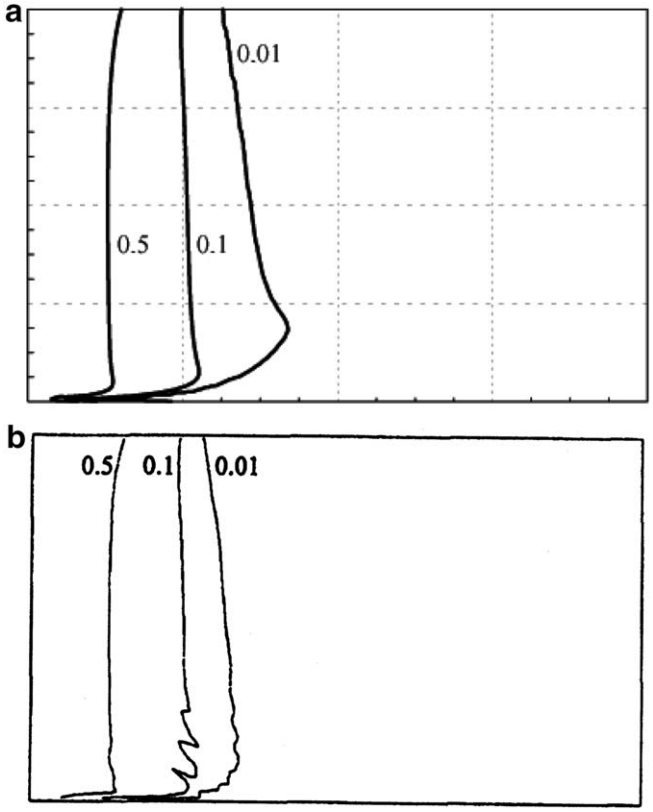

Fig. 8. Solid fraction isovalues after 100 s of solidification for experiment B: (a) our model and (b) FVM code in Ahmad et al. [29].

the enriched liquid flowing through the mush is collected. Fig. 8 shows the solid fraction isovalues calculated with the two models. Small solid volume fractions are found in the bottom of the domain. The structure of the concentration field is essentially different from the previous case due to the opposing convective effects. We show in Fig. 9 the concentration field obtained with our code and with the two codes presented in [29]. The results between our code (Fig. 9a) and the FEM code (Fig. 9b) are in good qualitative agreement, presenting enrichment in solute with a strong concentration gradient in the lower part of the enclosure. Note that a rather fine mesh is needed in the bottom region in order to correctly get the gradients of the different fields. For this calculation, a 80 horizontal $\times$ 48 vertical computational grid was used, with a refinement at the bottom: the function $H\cos(\pi/2)(i-1)/(49)$ was used for defining the ith position of the vertical sides of the meshes. For this particular case, λ_1 was used as the "pore size" in the Kozeny–Carman (Eq. 8) correlation. However, those two solutions disagree with the FVM simulation (Fig. 9c) which exhibits segregated channels in the inner part of the ingot. This discrepancy has been studied since the publication of the Ahmad et al. paper and a recent comparison [51] shows that FEM results on non-structured grids lead to the same kind of solution as Fig. 9c. If this is confirmed the present model will require further developments in terms of numerical accuracy. This kind of comparison also shows that there is a need of developing benchmark solutions for validating solidification models and the associated numerical codes.

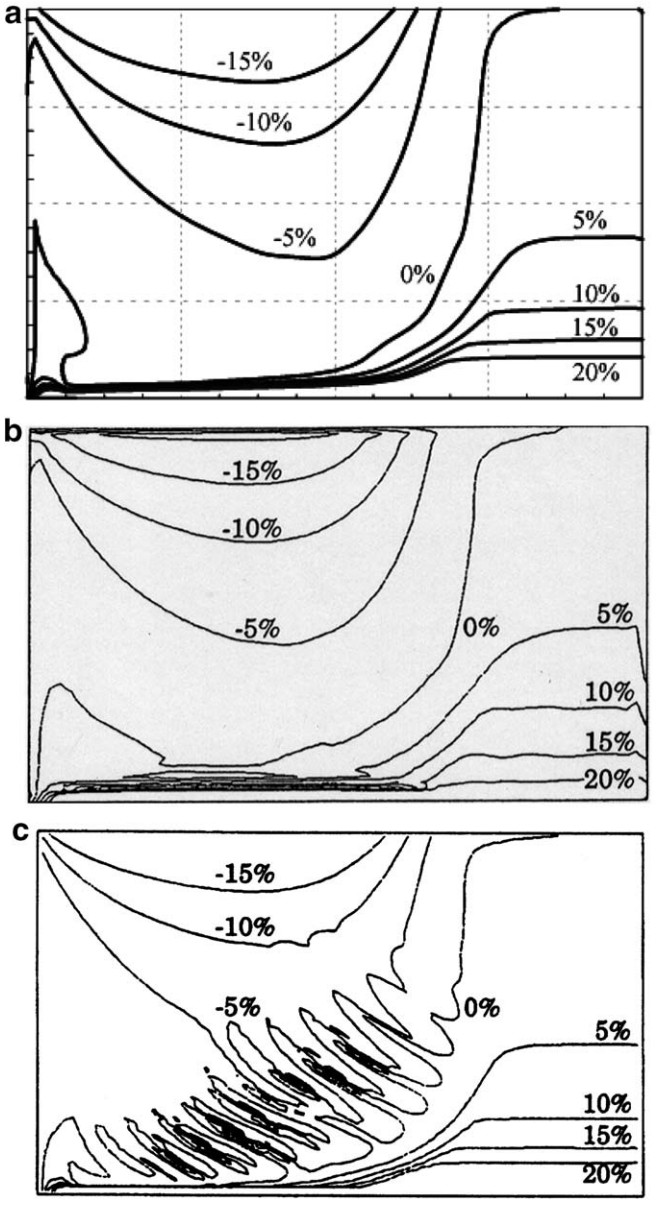

Fig. 9. Concentration enrichment isovalues in % after 400 s of solidification for experiment B: (a) our model, (b) FEM code in [29] and (c) FVM code in [29].

The simulations are compared to the experimental results from [30] in terms of relative mass fraction at the end of solidification in Fig. 10. For experiment A (Fig. 10a) the horizontal profile of relative tin mass fraction at 3.5 cm from the bottom of the cavity shows a fairly good agreement along the width of the domain, with a larger discrepancy along the insulated wall. In this respect the agreement is comparable with the results presented in [29]. A similar profile for the relative leads mass fraction for experiment B is represented in Fig. 10b. Again the average behavior is well represented, and the present solution is

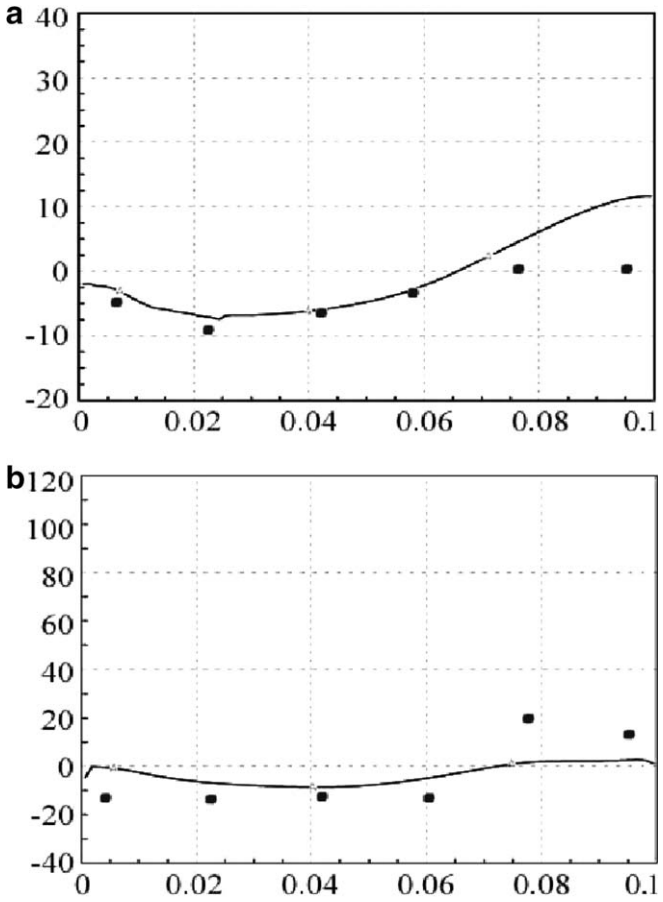

Fig. 10. Profiles of relative mass fraction at the end of solidification at 3.5 cm from the bottom. Comparison with experimental results [30]: (a) tin mass fraction for experiment A and (b) lead mass fraction for experiment B.

similar to the FEM solution presented in Ahmad et al. Similar results are obtained for the profiles at different heights and the results are consistant with the concentration fields presented in Fig. 9.

3.4.3. Experiment C: (Sn– 0% Bi)

In this experiment, due to the different mode of heat extraction (linear decrease in time of the cold wall temperature), solidification does not initiate immediately, and a relatively long period of thermal natural convection takes place before the beginning of solidification. The results are displayed in Fig. 11 at a solidification time of 300 s (left) and 600 s (right).

The calculations show formation of an horizontal channel that can be seen to increase in the solid fraction charts (Fig. 11a) at 300 and 600 s as more solid phase is produced. Lower solid fractions are found at the bottom of the domain. In addition to the solid fraction field, the streamlines are presented in Fig. 11b. They show that the flow intensity is much greater in the high porosity regions of the mushy zone, and that it decreases in time as the initial superheating decreases. The bottom part of the figure (Fig. 11c) displays the calculated macro-segregation field at the two instants, showing again the presence of the channel at the bottom of the enclosure. Similarly to experiment B, the lowest zone is enriched in solute. This is due to the additional effect of the solutal and thermal forces that causes the liquid flow to go down through the mushy zone. These observations are in good agreement with the experimental results reported by Quillet [31] as well as with his numerical calculations, in terms of concentration and temperature field. For conciseness reasons, these results are not recalled in the present document. We notice that the model in [31] shows some inclined freckles (two more freckles taking place). This might be due to the fact that the model used in this reference assumes solutal equilibrium (the average concentrations near the interface in both phases are equal to the equilibrium concentrations). This assumption favors freckles formation, as will be analyzed in Section 5 where a parametric study on species exchange coefficient is presented. The main interest of the solutal equilibrium model is that it is simple and gives good results for high diffusivities alloys. However, in the case of limited species diffusion alloys (such as stainless steel), this assumption of macro-scale solutal equilibrium may not be valid.

As a conclusion of these comparisons with existing numerical and experimental results in three different situations, we can underline that the numerical code based on the simplified "minimal" model of solidification for metallic binary alloys gives satisfactory results, in good agreement with different independent experiments and numerical models. A fully quantitative comparison is unfortunately difficult to perform, because the physical parameters required for such an accurate comparison between the model results and actual data are not available. This is certainly frustrating, but we believe that the proposed "validation" study justifies the use of the code for subsequent studies. We first have in mind the study of the possible influence of the porosity gradient terms. The idea is to perform several computations and extract from the results an order of magnitude of these correction terms, and decide if they might have significant effects. In this latter case, this would justify some extra programming effort to include the significant extra terms in the model. In addition, the same model may be used to test the sensitivity of the results to the effective properties of the mush. This is done in the next sections.

4. Influence of the non-classical terms

The purpose of the following section is to discuss the influence of the non-classical terms of the complete model, for the particular test-cases under consideration. For conciseness, the calculations are only presented for experiment B but the results apply to the other experiment cases. However, similar estimations would be necessary before extending the conclusions to very different solidification dynamics.

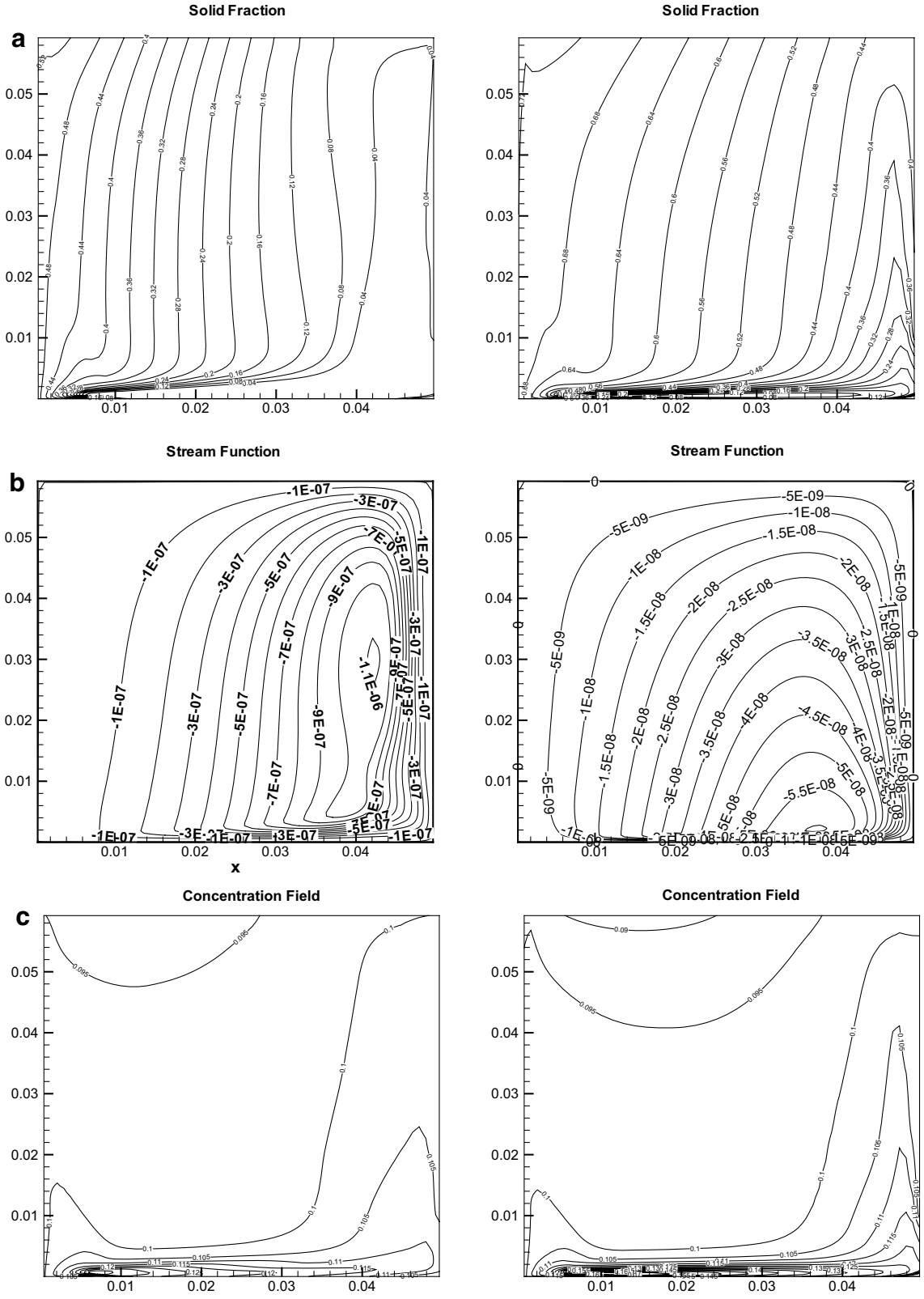

Fig. 11. Experiment C: (a) solid fraction, (b) streamlines and (c) concentration field (% in Bismuth) after 300 s (left) and 600 s (right) of solidification.

4.1. Brinkman correction terms

As previously said, Eq. (2) is characterized by the presence of the following three Brinkman terms ($\varepsilon_\ell \mu_\ell \nabla^2 \langle \vec{V}_\ell \rangle^\ell$, $\mu_\ell \vec{\nabla} \varepsilon_\ell . \vec{\nabla} \langle \vec{V}_\ell \rangle^\ell, \mu_\ell (\nabla^2 \varepsilon_\ell) \langle \vec{V}_\ell \rangle^\ell$). The first one represents the classical Brinkman correction term (corresponding to viscous diffusion effects) while the second and third terms involve porosity gradients which are related to the

heterogeneity of the columnar dendritic mushy zone. For the three test cases under consideration, these terms have been estimated on the basis of the numerical results obtained from the simplified model.

First, the second Brinkman term $(\mu_\ell \vec{\nabla}\varepsilon_\ell.\vec{\nabla}\langle\vec{V}_\ell\rangle^\ell)$ is compared to the Darcy friction term and to the first Brinkman correction term, respectively, which are the dominant terms in the momentum equation. The comparison is performed using the following ratios:

$$R_1 = \frac{|\vec{\nabla}\varepsilon_\ell.\vec{\nabla}\langle\vec{V}_\ell\rangle_x^\ell|}{|\varepsilon_\ell^2 K^{-1}\langle\vec{V}_\ell\rangle_x^\ell|}, \quad R_2 = \frac{|\vec{\nabla}\varepsilon_\ell.\vec{\nabla}\langle\vec{V}_\ell\rangle_z^\ell|}{|\varepsilon_\ell^2 K^{-1}\langle\vec{V}_\ell\rangle_z^\ell|} \tag{11}$$

$$R_3 = \frac{|\vec{\nabla}\varepsilon_\ell.\vec{\nabla}\langle\vec{V}_\ell\rangle_x^\ell|}{|\varepsilon_\ell\nabla^2\langle\vec{V}_\ell\rangle^\ell|}, \quad R_4 = \frac{|\vec{\nabla}\varepsilon_\ell.\vec{\nabla}\langle\vec{V}_\ell\rangle_z^\ell|}{|\varepsilon_\ell\nabla^2\langle\vec{V}_\ell\rangle^\ell|} \tag{12}$$

In Fig. 12, the spatial distribution of R_1 and R_2 are presented. It can be seen that both components of the second Brinkman correction term are small compared to the corresponding Darcy contribution (less than 0.01). It is interesting to note that the maximum values are reached for small solid volume fractions (less than 10%, see Fig. 8) i.e. at the vicinity of the top of the dendrites. This is also the region where the calculations of R_3 and R_4 (not reported here) have been found to be of the order 1. The same results were found for the two other test-cases.

In the same way, the third Brinkman term is compared to the Darcy term and to the first Brinkman correction using the ratios

$$R_5 = \frac{|\nabla^2\varepsilon_\ell\langle\vec{V}_\ell\rangle^\ell|}{|\varepsilon_\ell\nabla^2\langle\vec{V}_\ell\rangle^\ell|}, \quad R_6 = \frac{|\nabla^2\varepsilon_\ell|}{|\varepsilon_\ell^2 K^{-1}|} \tag{13}$$

R_5 and R_6 are calculated for the three experiment cases and results for experiment B are presented in Fig. 13. It is shown that R_5 can be on the order of 1 meaning that the third Brinkman term can have the same order of magnitude as the first one. As previously, these values are reached at the extremity of the dendrites and in the channel, where high porosity and porosity gradients are observed. Finally, R_6 is always found to be lower than 1% implying that the third Brinkman term is negligible in comparison to the Darcy term.

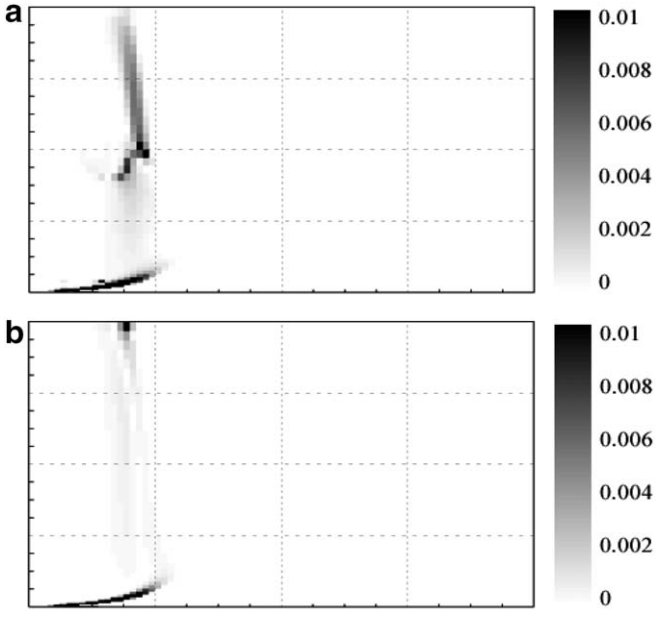

Fig. 12. Module of the ratio of the second Brinkman term to the Darcy term for experiment B after 50 s of solidification: (a) x component (R_1) and (b) z component (R_2).

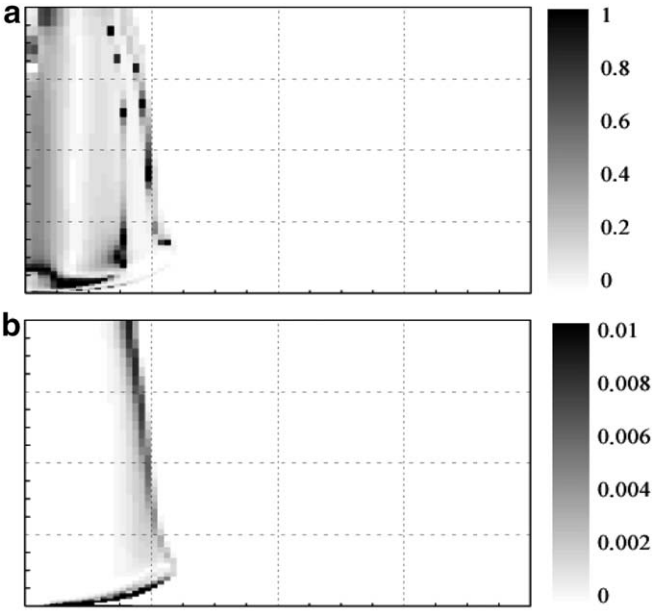

Fig. 13. (a) Ratio of third Brinkman term to first Brinkman term (ratio 5) and (b) module of the ratio of third Brinkman term to Darcy term for experiment B after 50 s of solidification (ratio 6).

In conclusion, as expected the second and the third Brinkman correction terms have been found to be small compared to the Darcy contribution while they can be of the same order of the viscous diffusion term especially close to the tip of the dendrite where the solid volume fraction is small. As a first approximation, these correction terms will be neglected.

4.2. Porosity gradient terms in species equations

The derivation of the macroscopic equation for the solidification rate and species conservation also brings up non-classical term involving porosity gradients. In this section, their order of magnitude are estimated through the use of the following ratios:

$$R_7 = \frac{|\rho_k D_k(\vec{\nabla}\varepsilon_k).\vec{\nabla}\langle C_k\rangle^k|}{|\rho_k h_{mk}(C_k^* - \langle C_k\rangle^k)|}, \quad R_8 = \frac{|\nabla.\rho_k D_k(\vec{\nabla}\varepsilon_k)(C_k^* - \langle C_k\rangle^k)|}{|\rho_k h_{mk}(C_k^* - \langle C_k\rangle^k)|} \tag{14}$$

For the three test-cases, both R_7 and R_8 ratios were found to be negligible in the solid and fluid phases. For example the maximum value for R_7 in the solid was of the order of 10^{-4} while it reached 10^{-3} in the core of the mushy zone.

4.3. Effect of the Péclet number

Solute dispersion phenomena are due to the correlated deviations of the velocity and of the species concentrations. These effects are generally more important in the direction of the flow than in the transverse direction. They depend on the intensity of the flow through the local Péclet number:

$$Pe = \frac{\langle \vec{V}_\ell \rangle^\ell l_k}{D_\ell} \tag{15}$$

where l_k is the characteristic length scale. In our case, l_k is chosen to be the first dendritic arm spacing λ_1. In order to study the influence of the flow intensity on the effective diffusion–dispersion coefficient, Bousquet-Melou et al. [26] solved the associated closure problem for non-chemical equilibrium model using schematic and digitized dendritic mushy zones. The classical Péclet-dependence was obtained, that is, for $Pe < 10$, the effective diffusion tensor is constant and mainly diffusive, while larger Péclet numbers give rise to important non-isotropic dispersion effects. Following these authors, the longitudinal and transverse dispersion coefficients $\mathbf{D}_{\ell_{xx}}$ and $\mathbf{D}_{\ell_{yy}}$ are respectively given by:

$$\frac{\mathbf{D}_{\ell_{xx}}}{\varepsilon_\ell D_\ell} = A_{xx} Pe^m, \quad \frac{\mathbf{D}_{\ell_{yy}}}{\varepsilon_\ell D_\ell} = A_{yy} Pe^m \tag{16}$$

where the m exponent was found to be close to 1.5 with a slight influence of the liquid fraction. The local Péclet number fields have been evaluated for the three test-cases and Fig. 14 shows the estimation for experiment B (Pb–5% Sn). The figure displays the horizontal distribution of the Péclet number (solid line) and of the solid fraction (dashed line) at mid-height of the enclosure. The representation is only provided within the mushy zone where dispersion effects may occur. As expected, for all the experiments, the larger values of the Péclet number ($Pe \geqslant 100$) are located at the vicinity of the tip of the dendrites where a strong flow intensity is observed. In order to quantify the dispersion effects, additional calculations were performed using a modified diffusion–dispersion tensor. Since in the dendritic mushy zone the fluid velocity is mainly orthogonal to the primary dendritic arm, the longitudinal dispersion is in the y-direction while the transverse one is in the horizontal x-direction. Following Bousquet-Melou et al. [26], $A_{xx} = 316 \times 10^{-2}$ and $A_{yy} = 3.16 \times 10^{-3}$. The results obtained for experiment C (Bi–Sn) show a very small influence of the dispersion coefficients on the solid fraction and macro-segregation fields (less than 1%). This is due to the macroscopic Péclet number ($\langle \vec{V}_\ell \rangle^\ell L / \mathbf{D}_{\ell_{xx}}$) which always remains greater than 1 in this experiment. Therefore, the solute transport is dominated by convection and the increase of the solute transport due to dispersion phenomena is not noticeable. Finally, in situations where dispersion effects are not negligible, it is important to note that they can have a stronger influence at the beginning of the process since the intensity of the convective flow reduces when solidification goes on.

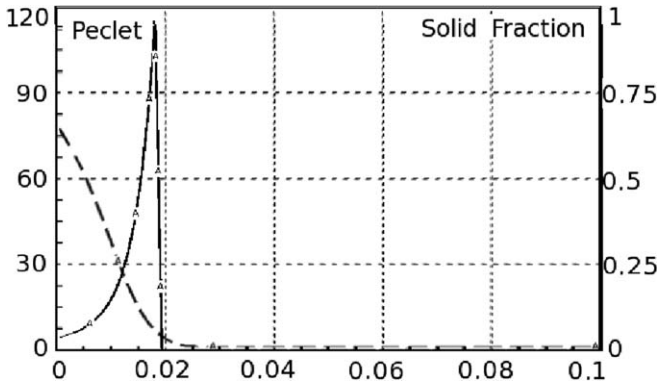

Fig. 14. Experiment B: Horizontal profile at mid-height of the local Péclet number (solid line), and of the solid fraction (dashed line) after 50 s of solidification.

5. Influence of permeability and interfacial mass exchange coefficients

This section concerns the estimation of the influence of the interfacial mass exchange coefficients and permeability on the solidification process. In order to illustrate the discussion, calculations were performed with parameters corresponding to experiment C.

5.1. Interfacial mass exchange coefficients

One of the originalities of the macroscopic model is related to the non-chemical equilibrium representation (difference between average and interfacial concentrations) of the solute transport. In terms of effective transport properties, this non-equilibrium is characterized by two interfacial species exchange coefficients whose influence on the solidification process is presented below. Numerical simulations were carried out using Eq. (17) which has been multiplied by a factor A

$$h_{mk} = A \times 12 \frac{D_k}{\lambda_2^2 \varepsilon_k} \tag{17}$$

In order to quantify the influence of h_{mk}, four values of this factor have been taken ($A = 0.1$, 1, 10, 20). As expected, for all experiments, the ratio $(\rho_s h_{m_s}(C_s^* - \langle C_s \rangle^s))/(\rho_\ell h_{m_\ell}(C_\ell^* - \langle C_\ell \rangle^\ell))$ was found to be much smaller than 1. This is due to the strong difference between the liquid and solid diffusion coefficients for metallic alloys ($D_\ell/D_s \approx 10^4$). Therefore, according to equation (6), the phase change rate is mainly controlled by the interfacial solute exchange coefficient in the liquid phase.

For all the experiments presented in the previous section, the ratios $(C_s^* - \langle C_s \rangle^s)/(\langle C_s \rangle^s)$ and $(C_\ell^* - \langle C_\ell \rangle^\ell)/(\langle C_\ell \rangle^\ell)$ are calculated in order to quantify the deviation from equilibrium. In the liquid phase, the larger the exchange coefficients, the closer the system is to local-equilibrium ($A = 0.1$ leads to a 5% deviation from equilibrium,

while $A = 20$ only leads to 0.03%). It seems that a change in h_{ml} is made up by a change in the amount of non-equilibrium. This would explains the small influence of the interfacial solute exchange coefficient on the solidification rate that has been observed in our computations. At the contrary to the liquid phase, a large deviation from equilibrium is observed in the solid phase (~10%) but this has been found to be independent on the exchange coefficient.

The influence of h_{ml} on the solid fraction field is illustrated on Fig. 15. It can be observed that the solid fraction is hardly influenced by the interfacial exchange coefficient, except at the bottom of the cavity where the solute concentration has been found to be more important. The influence on the segregation field after 600 s of solidification is also plotted in Fig. 16. Differences between $A = 0.1$ and $A = 20$ are significant and the 0% segregation isovalue shows the presence of a freckle for $A = 20$. Finally, it has been observed that an increase in the exchange coefficient increases the amplitude of macro-segregation. For instance, when $A = 0.1$, macro-segregation (after 600 s of solidification) ranges from 9% to 15.74% while $A = 1$ ranges from 8.9% to 17.37%. This change seems to be due to equilibrium. Indeed, when the macroscopic concentration field is close to equilibrium, a strong micro-segregation between the solid and the liquid phases takes place and natural convection in the liquid phase gives rise to a macroscopic solute redistribution.

5.2. Influence of permeability

In order to evaluate the influence of permeability, computations have been performed using the Kozeny–Carman Eq. (8) which has been multiplied by 0.1, 10 or 100. For experiment C, the reference value has been obtained for $A = 1$ where the macro-segregation field ranges from 8.9% to 17.37%. When Eq. (8) is multiplied by 0.1 this range reduces (9.67–10.92%) while it is significantly enlarged when permeability is multiplied by a factor 10 (6.9%–18.5%). This larger macro-segregation range is due to the increase of convective flow intensity in the mushy zone giving rise to a larger macroscopic solute redistribution. The influence of permeability was also carried out for both moderate ($A = 10$) and strong $A = 1$ deviations to solutal equilibrium. It that latter case, it was observed that a significant increase of permeability (factor 100) leads to a moderate change of the solid volume fraction field. At the contrary, close to the chemical equilibrium ($A = 10$), changes of the permeability strongly affect the solid volume fraction (Fig. 17). Indeed, it is shown that increasing the permeability can produce freckles in regions where enriched liquid is collected.

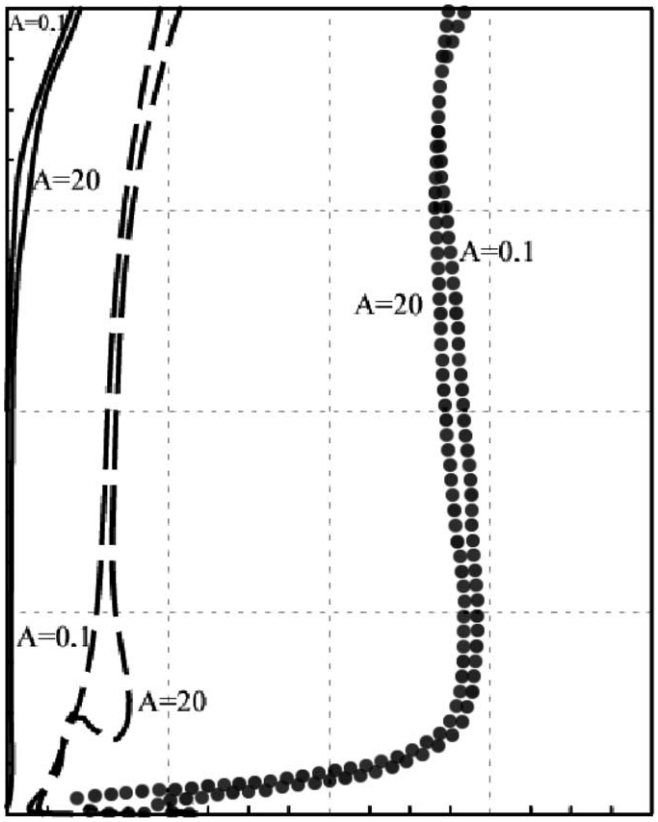

Fig. 15. Isovalues of solid fraction for $A = 0.1$, $A = 20$ after 300 s of solidification experiment C. (solid fraction = 0.5 (solid line), 0.4 (dashed line) and 0.1 (dotted line)).

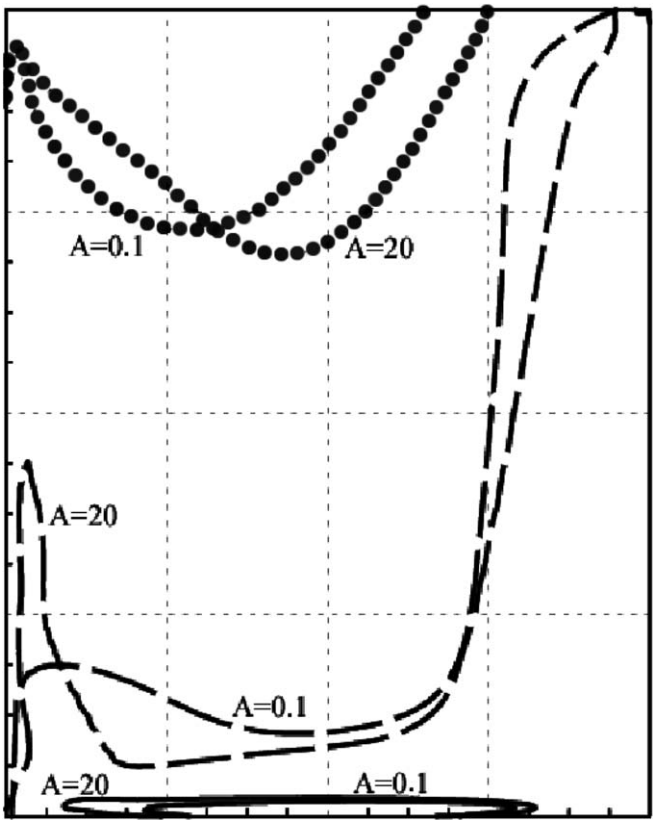

Fig. 16. Isovalues of macro-segregation after 600 s of solidification for $A = 0.1$ and $A = 20$ for experiment C. (−5% (dotted line), 0% (dashed line), 35% (solid line)).

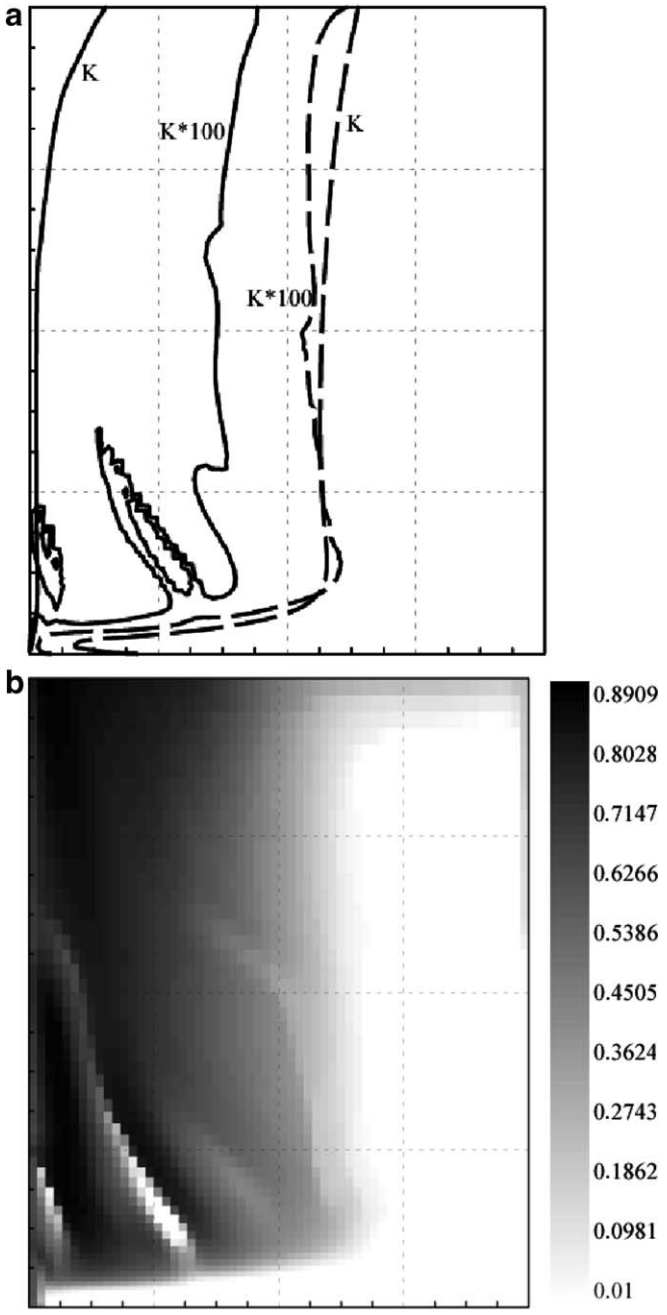

Fig. 17. Influence of the permeability on the solid volume fraction field for Experiment C ($A = 10$): (a) solid fraction isolines: 0.3 (dashed line) and 0.6 (solid line) and (b) Solid fraction field for a permeability multiplied by a factor 100.

6. Conclusion

In this paper a macroscopic model of columnar dendritic solidification of binary mixtures has been presented and implemented. This model, derived by a volume averaging technique, is first characterized by extra terms involving porosity gradients standing for the spatial variation of the pore-scale geometry and second by a macroscale non-equilibrium representation accounting for chemical exchanges at the solid–liquid interface. Due to the complexity of this model, a simplified version, without porosity gradient terms, has been implemented. Numerical simulations have been compared to the numerical and experimental results of three metallic alloys solidification cases available in the literature. Globally, these comparisons have been found to be in good qualitative agreement with the previous results but further numerical developments are found to be necessary. Porosity extra terms were systematically estimated on the basis of these numerical simulations. They were found to be negligible except in the limited zone at the vicinity of the dendrites tip. However, we must keep in mind that the possible influence of the porosity gradient terms on the macroscopic fields has not been evaluated and that numerical simulations using the full model, including these terms are still necessary. In order to study the solute dispersion effects, the local Péclet number fields have been evaluated for the three test-cases. In all cases, large values of the Péclet number were found at the vicinity of the tip of the dendrites but a very small influence of the dispersion coefficients on the solid fraction and macro-segregation fields was observed. Finally, the influence on solidification of effective transport properties such as permeability and interfacial solute exchange coefficients have been investigated. It was found that both parameters have a strong influence on macro-segregation and solid fraction fields. Indeed, a lower(larger) permeability gives rise to a weaker(stronger) convective regime and therefore to a more uniform(non-uniform) solute segregation field. A significant influence of the permeability tensor on freckle formation was also observed. The influence of the interfacial solute exchange coefficients on the deviation from chemical equilibrium has been emphasized. As expected, in the liquid phase, the larger the mass exchange coefficients, the closer the system is to local chemical equilibrium. This increases the amplitude of macro-segregation, and freckle formation has been observed. All these results confirm the need to account for chemical non-equilibrium in macroscopic solidification modeling and to accurately define the average properties transport.

References

[1] R. Wright, Core melt progression: status of current understanding and principal uncertainties, Rogers J.T., 1996.
[2] W. Kurz, D. Fisher, Fundamentals of Solidification, Trans Tech Publications, 1992.
[3] M. Flemings, Solidification Processing, McGraw-Hill, 1974.
[4] W. Bennon, F. Incropera, A continuum model for momentum heat and species transport in binary solid–liquid phase change systems (1) model formulation, Int. J. Heat Mass Transfer 30 (1987) 2161–2170.
[5] W. Bennon, F. Incropera, A continuum model for momentum heat and species transport in binary solid-liquid phase change systems (2) application to solidification in a rectangular cavity, Int. J. Heat Mass Transfer 30 (1987) 2171–2187.
[6] V. Voller, C. Prakash, A fixed grid numerical modelling methodology for convection–diffusion mushy region phase-change problems, Int. J. Heat Mass Transfer 30 (1987) 1709–1719.
[7] V. Voller, C. Prakash, The modelling of heat mass and solute transport in solidification systems, Int. J. Heat Mass Transfer 32 (1989) 1719–1731.

[8] J. Auriault, P. Adler, Taylor dispersion in porous media: analysis by multiple scale expansions, Adv. Water Resour. 18 (1995) 217–226.
[9] S. Torquato, Random Heterogeneous Materials Microstructure and Macroscopic Properties, Springer-Verlag, 2002.
[10] S. Whitaker, The Method of Volume Averaging, Kluwer Academic Publishers, 1999.
[11] C. Beckermann, R. Viskanta, Double-diffusive convection during dendritic solidification of a binary mixture, Physicochem. Hydrodyn. 10 (1988) 195–213.
[12] S. Ganesan, D. Poirier, Conservation of mass and momentum for the flow of interdendritic liquid during solidification, Metall. Trans. B 21B (1990) 173–181.
[13] J. Ni, C. Beckermann, A volume-averaged two-phase model for transport phenomena during solidification, Metall. Trans. B 22B (1991) 349–361.
[14] M. Schneider, C. Beckermann, Formation of macrosegregation by multicomponent thermosolutal convection during the solidification of steel, Metall. Mater. Trans. A 26A (1995) 2373–2388.
[15] C. Wang, C. Beckermann, Equiaxed dendritic solidification with convection. Part 1: multiscale/multiphase modelling, Metall. Mater. Trans. A 27 A (1996) 2754–2764.
[16] J. Gu, C. Beckermann, Simulation of convection and macrosegregation in a large steel ingot, Metall. Mater. Trans. 30A (1999) 1357–1366.
[17] B. Goyeau, T. Benihaddadene, D. Gobin, M. Quintard, Averaged momentum equation for flow through a non homogeneous porous structure, Transp. Porous Media 28 (1997) 19–50.
[18] B. Goyeau, P. Bousquet-Melou, D. Gobin, M. Quintard, F. Fichot, Macroscopic modeling of columnar dendritic solidification, Comput. Appl. Math. 23 (2–3) (2004) 381–400.
[19] S. Whitaker, Flow in porous media 1: a theoretical derivation of Darcy's law, Transp. Porous Media 1 (1986) 3–25.
[20] M. Quintard, S. Whitaker, Transport in ordered and disordered porous media II: generalized volume averaging, Chem. Eng. Sci. 14 (48) (1993) 2537–2564.
[21] M. Quintard, S. Whitaker, Transport in ordered and disordered porous media III: closure and comparison between theory and experiment, Transp. Porous Media 15 (1994) 31–49.
[22] P. Prescott, F. Incropera, Numerical simulation of a solidifying Pb–Sn alloy: the effects of cooling rate on thermosolutal convection and macrosegregation, Metall. Trans. B 22B (1991) 529–540.
[23] P. Prescott, F. Incropera, D. Gaskell, Convective transport phenomena macrosegregation of a binary metal alloy: 2. experiments and comparisons with numerical predictions, J. Heat Transfer 116 (1994) 742–749.
[24] M. Rappaz, V. Voller, Modelling of micro-macrosegregation in solidification processes, Metall. Trans. A 21A (1990) 749–753.
[25] D. Poirier, P. Nandapurkar, S. Ganesan, The energy and solute conservation equations for dendritic solidification, Metall. Trans. B 22B (1991) 889–900.
[26] P. Bousquet-Melou, A. Neculae, B. Goyeau, M. Quintard, Average solute transport during solidification of a binary mixture: active dispersion in dendritic structures, Metall. Mater. Trans. 33B (2002) 365–376.
[27] C. Wang, C. Beckermann, A multiphase solute diffusion model for dendritic alloy solidification, Metall. Trans. A 24 A (1993) 2787–2802.
[28] C. Wang, C. Beckermann, Prediction of columnar to equiaxed transition during diffusion-controlled dendritic alloy solidification, Metall. Mater. Trans. A 25A (1994) 1081–1093.
[29] N. Ahmad, H. Combeau, J. Desbiolles, T. Jalanti, G. Lesoult, J. Rappaz, M. Rappaz, C. Stomp, Numerical simulation of macrosegregation: a comparison between finite volume method and finite element method prediction and a confrontation with experiments, Metall. Mater. Trans. 29A (1998) 617–630.
[30] D. Hebditch, J. Hunt, Observations of ingot macrosegregation on model systems, Metall. Trans. 5 (1974) 1557–1564.
[31] G. Quillet, Influence de la convection, naturelle ou forcée, sur l'apparition des mésoségrégations lors de la solidification d'alliages métalliques, Ph.D. thesis, Institut National Polytechnique de Grenoble, 2003.
[32] P. Bousquet-Melou, B. Goyeau, M. Quintard, F. Fichot, D. Gobin, Average momentum equation for interdendritic flow in a solidifying columnar mushy zone, Int. J. Heat Mass Transfer 45 (2002) 3651–3665.
[33] J.A. Ochoa-Tapia, S. Whitaker, Momentum transfer at the boundary between a porous medium and a homogeneous fluid (1) theoretical development, Int. J. Heat Mass Transfer 38 (1995) 2635–2646.
[34] J.A. Ochoa-Tapia, S. Whitaker, Heat transfer at the boundary between a porous medium and a homogeneous fluid, Int. J. Heat Mass Transfer 46 (1997) 2691–2707.
[35] B. Goyeau, D. Lhuillier, D. Gobin, M. Velarde, Momentum transport at a fluid-porous interface, Int. J. Heat Mass Transfer 46 (2003) 4071–4081.
[36] S. Whitaker, The Forchheimer equation: a theoretical development, Transp. Porous Media 25 (1996) 27–61.
[37] S. Ganesan, C. Chan, D. Poirier, Permeability for flow parallel to primary dendrite arms, Mater. Sci. Eng. A151 (1992) 97–105.
[38] B. Goyeau, T. Benihaddadene, D. Gobin, M. Quintard, Numerical calculation of the permeability in a dendritic mushy zone, Metall. Mater. Trans. B 30 B (1999) 613–622.
[39] A. Neculae, B. Goyeau, M. Quintard, D. Gobin, Passive dispersion in dendritic structures, Mater. Sci. Eng. A323 (2002) 367–376.
[40] M. Quintard, S. Whitaker, One- and two-equation models for transient diffusion processes in two-phase systems, Adv. Heat Transfer 23 (1993) 369–464.
[41] M. Quintard, S. Whitaker, Local thermal equilibrium for transient heat conduction: theory and comparison with numerical experiments, Int. J. Heat Mass Transfer 38 (1995) 2779–2796.
[42] M. Quintard, M. Kaviany, S. Whitaker, Two-medium treatment of heat transfer in porous media: numerical results for effective properties, Adv. Water Resour. 20 (1997) 77–94.
[43] J. Bear, Dynamics of Fluids in Porous Media, Dover, 1972.
[44] M. Schneider, J. Gu, C. Beckermann, W. Boettinger, U. Kattner, Modeling of micro- and macrosegregation and freckle formation in single-crystal nickel-base superalloy directional solidification, Metall. Mater. Trans. A 28 A (1997) 1517–1531.
[45] R. Nasser-Rafi, R. Deshmukh, D. Poirier, Flow of interdendritic liquid and permeability in Pb-20% wt Sn alloys, Metall. Trans. A 16 A (1985) 2263–2271.
[46] D. Poirier, Permeability for flow of interdendritic liquid in columnar-dendritic alloys, Metall. Trans. B 18A (1987) 245–255.
[47] C. Beckermann, C. Wang, Multiphase/scale modeling of alloy solidification, Ann. Rev. Heat Transfer 6 (1995) 115–198.
[48] M. Quintard, S. Whitaker, Two-phase flow in heterogeneous porous media: the method of large-scale averaging, Transp. Porous Media 3 (1988) 357–413.
[49] P. Thevoz, M. Rappaz, J.-L. Desbiolles, 3-MOS: a general FEM code for the prediction of microstructures in castings, in: C.M. Bickert (Ed.), Light Metals, TMS, Warrendale, PA, 1990, pp. 975–984.
[50] I. Vannier, H. Combeau, G. Lesoult, Numerical model for prediction of the final segregation pattern of bearing steel ingots, Mater. Sci. Eng. A 173 (1993) 317–321.
[51] W. Liu, Finite element modelling of macrosegregation and thermo-mechanical phenomena in solidification process, Ph.D. thesis, Ecole des Mines, Sophia-Antipolis, 2005.